Geophysical Journal International

Geophys. J. Int. (2021) **225,** 1378–1391
Advance Access publication 2021 January 25
GJI Seismology

doi: 10.1093/gji/ggab032

Internal co-seismic displacement and strain changes inside a homogeneous spherical Earth

Jie Dong,[1] Pengfei Cheng,[1] Hanjiang Wen[1] and Wenke Sun[2]

[1]*Chinese Academy of Surveying and Mapping, Beijing* 100036, *China. E-mail: dongmei731@163.com*
[2]*Key Laboratory of Computational Geodynamics, University of Chinese Academy of Sciences, Beijing* 100049, *China*

Accepted 2021 January 20. Received 2021 January 20; in original form 2020 December 2

SUMMARY

In this study, we devised a new set of analytical foundation solutions to compute the internal co-seismic displacement and strain changes caused by four independent point sources (strike-slip, dip-slip, horizontal tensile and vertical tensile) inside a homogeneous spherical earth model. Our model provides constraints on the deformation properties at depth and reveals that the internal co-seismic deformation is larger than that on the surface. The deformation near the source is convergent with our formulae. For the internal deformation at radial section plane, the patterns of horizontal displacements u_θ, u_ϕ and strain changes e_{rr}, $e_{\theta\theta}$, $e_{\phi\phi}$, $e_{\theta\phi}$ caused by strike-slip and tensile sources appear symmetric at the equidistance above and below the source. Their amplitudes are not identical but with a small discrepancy actually. Unlike these, the patterns of radial displacements u_r for strike-slip and tensile sources exhibit point symmetry with the equidistance from the source. Also, the corresponding amplitudes are slightly different. The displacements u_θ, u_ϕ and strain changes e_{rr}, $e_{\theta\theta}$, $e_{\phi\phi}$, $e_{\theta\phi}$ caused by dip-slip also show the same properties as u_r of the strike-slip source. The magnitudes of the displacements and strain changes depend on the source types. The curvature effect on the near-field surface deformations is small, and it increases with the studied depth. However, for the far-field deformation caused by the strike-slip source ($d_s = 20$ km), the curvature effect can be as large as 77 per cent when the epicentral distance approximates to 1778 km.

Key words: Seismic cycle; Numerical solutions; Planetary interiors; Computational seismology; Theoretical seismology.

1 INTRODUCTION

Earthquakes can cause significant deformation at both the surface and internal layers. With the development of seismology, not only the surface co-seismic deformation has been studied, but also the internal deformation inside an Earth attracts attention. Internal deformation is related to the earthquake triggering mechanism. Especially for the seismic cycle, the accumulation and release of stress within the Earth can affect or trigger aftershocks and later seismic events. Shan *et al.* (2009) conducted a surface deformation study of the Wenchuan earthquake (M_w7.9) in order to calculate the stress changes and to predict the location of potential aftershocks. The high-precision geodetic observations on the surface can validate the computing surface deformation. While it is difficult to observe the internal deformation directly, it is possible to create internal deformation models based on dislocation theory.

The dislocation theory has evolved from a simple half-space model to a more realistic spherical model. Okada (1985) presented a set of simple analytical formulae to calculate the surface co-seismic displacement and strain changes in the homogeneous elastic half-space earth model, which is still widely used because of its mathematical simplicity. Okubo (1992) gave analytical formulae for calculating the gravitational potential and gravitational change of the medium model in a half-space model. Later, many works have explored the potential of the layered half-space model (Singh 1970; Jovanovich *et al.* 1974a,b; Matsu'ura *et al.* 1981; Ma & Kusznir 1992; Ma & Lee 2009; Barbot & Fialko 2010a,b), which is more accurate than some of its predecessors. Wang *et al.* (2003, 2006) considered the radial structure of the Earth, improved the dislocation theory of the half-space model and provided an effective scheme for calculating co-seismic and post-seismic deformation caused by any point source or generalized finite fault source. Furthermore, the material anisotropy effect (Pan *et al.* 2014) has been incorporated into dislocation theory. The dislocation theory has also been applied to more realistic spherical earth models (Ben-Menahem & Singh 1968; Ben-Menahem *et al.* 1969, 1970). The spherically symmetric, non-rotating, perfectly elastic and isotropic (SNREI; Dahlen 1968) earth model considers the curvature and stratification structures of the Earth. Sun & Okubo (1993) calculated the surface seismic deformation based on the SNREI model. Many researchers (Piersanti *et al.* 1995, 1997; Sabadini *et al.* 1995; Pollitz 1996; Sabadini & Vermeersen

1997; Soldati *et al.* 1998; Shen *et al.* 2019) calculated the surface deformation using another spherical model—normal model, which is an uncompressible earth model. For the post-seismic relaxation computation, researchers (Pollitz *et al.* 2006; Tanaka *et al.* 2006, 2007) also inclined to the spherically stratified, compressible and self-gravitating viscoelastic earth model. Moreover, the load deformation (Longman 1962, 1963; Farrell 1972; Pan 1989) and slip distribution inversions (Pollitz *et al.* 2011; Zhou *et al.* 2014, 2018) are based on dislocation theory. Pan (2019) gives a review of the Green's functions for layered sphere and layered half-space. While the above studies developed robust surface deformation calculations, they do not address the internal deformation; very few studies do. Although Okada (1992) presented a set of analytical formulae to calculate the internal co-seismic deformation, it is based on a half-space earth model. Casarotti *et al.* (2001) developed the model of viscoelastic post-seismic deformation based on a normal model and discussed the effect of the stress transferred on the fault interaction inside a spherical Earth. Takagi & Okubo (2017) presented a new method to compute the internal deformations by introducing the asymptotic solutions of the radial functions to avoid the non-convergence near the dislocation, which is summed up by the deform factors with spherical harmonic degree.

In our study, we investigate the internal deformation in a homogeneous spherical model (SNREI) by summing up the spherical harmonics using a new set of analytical foundation solutions derived, which are different from Takagi & Okubo (2017) using the solutions of Love (1911). Our straightforward approach does not involve non-convergence near the source. By exactly computing high harmonic degrees avoiding any approximation error, we can determine the internal Green's functions and draw conclusions about the internal deformation. This is an important step towards the internal deformation research on the radial stratification spherical earth model, because the internal structure also affects the co-seismic deformation (Fu & Sun 2007; Dong *et al.* 2021). Furthermore, it can enhance our understanding of the stress status, mass redistribution and focal mechanism in the seismic cycle.

2 COMPUTING METHODS

2.1 Fundamental equations for internal co-seismic deformations in a homogeneous spherical Earth

Based on the homogeneous spherical earth model (SNREI), we calculate the internal co-seismic deformation caused by a point source (S). We use the spherical coordinates (r, θ, ϕ), where r is the geocentric distance, and θ and ϕ are the co-latitude and longitude, respectively. The co-seismic displacement ($\boldsymbol{u}$) and stress ($\boldsymbol{\tau}$) are excited by a unit point source ($\boldsymbol{f}$) at a location (r_0, θ_0, ϕ_0) that satisfies the equations of equilibrium and stress–strain relation (Alterman *et al.* 1959; Takeuchi & Saito 1972):

$$\nabla \cdot \boldsymbol{\tau} + \rho \boldsymbol{f} = 0, \tag{1}$$

$$\boldsymbol{\tau} = \lambda \boldsymbol{I} \nabla \cdot \boldsymbol{u} + \mu \left(\nabla \boldsymbol{u} + (\nabla \boldsymbol{u})^{\mathrm{T}} \right), \tag{2}$$

where $\boldsymbol{I}$ is the unit tensor, superscript T stands for transpose, and μ and λ are the Lame constants of the Earth.

Generally, any function can be expressed as spherical harmonics on a unit sphere. The co-seismic displacement $\boldsymbol{u}(r, \theta, \phi)$ and stress $\boldsymbol{\tau}(r, \theta, \phi)$ can be expressed as

$$\boldsymbol{u}(r, \theta, \phi) = \sum_{n,m} \left[y_1(r) \boldsymbol{R}_n^m(\theta, \phi) + y_3(r) \boldsymbol{S}_n^m(\theta, \phi) + y_1^{\mathrm{t}}(r) \boldsymbol{T}_n^m(\theta, \phi) \right], \tag{3}$$

$$\boldsymbol{\tau} \cdot \boldsymbol{e_r}(r, \theta, \phi) = \sum_{n,m} \left[y_2(r) \boldsymbol{R}_n^m(\theta, \phi) + y_4(r) \boldsymbol{S}_n^m(\theta, \phi) + y_2^{\mathrm{t}}(r) \boldsymbol{T}_n^m(\theta, \phi) \right], \tag{4}$$

where y_1, y_2, y_3 and y_4 are the factors of spheroidal deformation. y_1 and y_3 stand for the radial and horizontal components of displacements. y_2 and y_4 stand for the radial and horizontal components of stresses. The superscript 't' stands for the toroidal deformation.y_1^{t} and y_2^{t} are the toroidal displacement and the stress, respectively. $\boldsymbol{R}_n^m(\theta, \phi)$, $\boldsymbol{S}_n^m(\theta, \phi)$ and $\boldsymbol{T}_n^m(\theta, \phi)$ are vector spherical functions and can be expressed as

$$\begin{aligned}
\boldsymbol{R}_n^m(\theta, \phi) &= \boldsymbol{e}_r Y_n^m(\theta, \phi), \\
\boldsymbol{S}_n^m(\theta, \phi) &= \left[\boldsymbol{e}_\theta \frac{\partial}{\partial \theta} + \boldsymbol{e}_\phi \frac{1}{\sin\theta} \frac{\partial}{\partial \phi} \right] Y_n^m(\theta, \phi), \\
\boldsymbol{T}_n^m(\theta, \phi) &= \left[\boldsymbol{e}_\theta \frac{1}{\sin\theta} \frac{\partial}{\partial \phi} - \boldsymbol{e}_\phi \frac{\partial}{\partial \theta} \right] Y_n^m(\theta, \phi),
\end{aligned} \tag{5}$$

with

$$\begin{aligned}
Y_n^m(\theta, \phi) &= P_n^m(\cos\theta) \mathrm{e}^{\mathrm{i}m\phi}, \\
Y_n^{-|m|}(\theta, \phi) &= (-1)^m P_n^{|m|}(\cos\theta) \mathrm{e}^{-\mathrm{i}|m|\phi}, \\
m &= 0, \pm 1, \pm 2, \ldots, \pm n,
\end{aligned} \tag{6}$$

where $P_n^m(\cos\theta)$ are the associated Legendre's functions. $(\boldsymbol{e_r}, \boldsymbol{e}_\theta, \boldsymbol{e}_\phi)$ are the base vectors in spherical coordinate for radial, co-latitude and longitude directions, respectively.

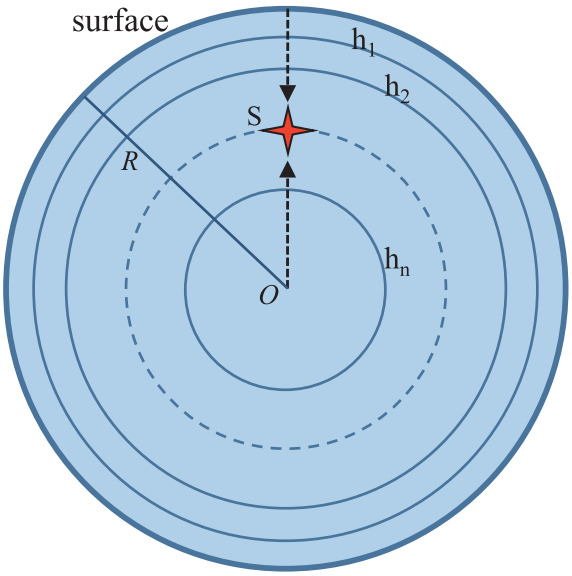

Figure 1. Sketch showing the source position (S) and internal spheres at $h_k (k = 1,\ 2,\ \ldots,\ n)$. R is the radius and O is the centre of the Earth.

Similarly, the point force $\boldsymbol{f}$ can be expressed as spherical harmonics:

$$\rho \boldsymbol{f} = \frac{\delta(r-r_0)}{r_0^2} \sum_{n,m} \left[F_2(r) \boldsymbol{R}_n^m(\theta,\phi) + F_4(r) \boldsymbol{S}_n^m(\theta,\phi) + F_2^{\mathrm{t}}(r) \boldsymbol{T}_n^m(\theta,\phi) \right], \tag{7}$$

with

$$\begin{aligned} F_2(r) &= \frac{2n+1}{4\pi} \frac{(n-m)!}{(n+m)!} \boldsymbol{R}_n^{m*}(\theta_0,\phi_0) \cdot \boldsymbol{v}, \\ F_4(r) &= \frac{2n+1}{4\pi n(n+1)} \frac{(n-m)!}{(n+m)!} \boldsymbol{S}_n^{m*}(\theta_0,\phi_0) \cdot \boldsymbol{v}, \\ F_2^t(r) &= \frac{2n+1}{4\pi n(n+1)} \frac{(n-m)!}{(n+m)!} \boldsymbol{T}_n^{m*}(\theta_0,\phi_0) \cdot \boldsymbol{v}, \end{aligned} \tag{8}$$

where $*$ stands for complex conjugate and $\boldsymbol{v}$ is a unit vector.

Substituting formulae (3), (4) and (7) into (1) and (2), and neglecting the gravity effect ($g = 0$), we obtain four ordinary spheroidal differential equations (9) and two toroidal equations (10) as

$$\begin{cases} \dfrac{\mathrm{d}y_1}{\mathrm{d}r} = \dfrac{1}{\beta}\left\{ y_2 - \dfrac{\lambda}{r}\left[2y_1 - n(n+1)y_3 \right] \right\} \\ \dfrac{\mathrm{d}y_2}{\mathrm{d}r} = \dfrac{4}{r}\left(\dfrac{3\kappa\mu}{r\beta} \right) y_1 - \dfrac{4\mu}{r\beta} y_2 - \dfrac{n(n+1)}{r}\left(\dfrac{6\mu\kappa}{r\beta} \right) y_3 + \dfrac{n(n+1)}{r} y_4 - F_2 \dfrac{\delta(r-r_0)}{r_0^2} \\ \dfrac{\mathrm{d}y_3}{\mathrm{d}r} = \dfrac{1}{\mu} y_4 - \dfrac{1}{r}(y_1 - y_3) \\ \dfrac{\mathrm{d}y_4}{\mathrm{d}r} = -\dfrac{6\mu\kappa}{r^2\beta} y_1 - \dfrac{\lambda}{r\beta} y_2 + \left\{ \dfrac{2\mu}{r^2\beta}\left[\left(2n^2+2n-1\right)\lambda + 2\left(n^2+n-1\right)\mu \right] \right\} y_3 \\ \qquad -\dfrac{3}{r} y_4 - F_4 \dfrac{\delta(r-r_0)}{r_0^2} \end{cases} \tag{9}$$

$$\begin{cases} \dfrac{\mathrm{d}y_1^{\mathrm{t}}}{\mathrm{d}r} = \dfrac{1}{r} y_1^{\mathrm{t}} + \dfrac{1}{\mu} y_2^{\mathrm{t}} \\ \dfrac{\mathrm{d}y_2^{t}}{\mathrm{d}r} = \dfrac{\mu(n-1)(n+2)}{r^2} y_1^{\mathrm{t}} - \dfrac{3}{r} y_2^{\mathrm{t}} - F_2^{\mathrm{t}} \dfrac{\delta(r-r_0)}{r_0^2}, \end{cases} \tag{10}$$

where $\beta = \lambda + 2\mu$ and $\kappa = \lambda + \frac{2}{3}\mu$.

Then, we derive the foundation solutions by eqs (9) and (10) and get four sets of spheroidal foundation solutions $y_{ji} (i,\ j = 1, 2, 3, 4)$ and two sets of toroidal foundation solutions $y_{ji}^{\mathrm{t}} (i,\ j = 1, 2)$.

In our study, we use the new foundation solutions to compute the internal displacement and stress at arbitrary depths $h_1, h_2, \ldots, h_{\mathrm{n}}$ (Fig. 1), which is different from the surface deformation calculation by Dong *et al.* (2016).

There are four sets of spheroidal solutions, two regular and two irregular, which depend on the normalized distance ($r = r/R$). The formulae are presented as eq. (11):

$$\begin{pmatrix} y_{11}(r) & y_{12}(r) & y_{13}(r) & y_{14}(r) \\ y_{21}(r) & y_{22}(r) & y_{23}(r) & y_{24}(r) \\ y_{31}(r) & y_{32}(r) & y_{33}(r) & y_{34}(r) \\ y_{41}(r) & y_{42}(r) & y_{43}(r) & y_{44}(r) \end{pmatrix} = \begin{pmatrix} -(n+1)r^{-n-2} & -\left[\dfrac{(n+1)\lambda+(n+3)\mu}{(n-2)\lambda+(n-4)\mu}\right]nr^{-n} & \dfrac{n\lambda+(n-2)\mu}{(n+3)\lambda+(n+5)\mu}(n+1)r^{n+1} & nr^{n-1} \\ 2\mu(n+1)(n+2)r^{-n-3} & \dfrac{(n^2+3n-1)\lambda+n(n+3)\mu}{(n-2)\lambda+(n-4)\mu}2\mu nr^{-n-1} & \dfrac{(n^2-n-3)\lambda+(n^2-n-2)\mu}{(n+3)\lambda+(n+5)\mu}2\mu(n+1)r^{n} & 2\mu n(n-1)r^{n-2} \\ r^{-n-2} & r^{-n} & r^{n+1} & r^{n-1} \\ -2\mu(n+2)r^{-n-3} & -\dfrac{(n^2-1)\lambda+(n^2-2)\mu}{(n-2)\lambda+(n-4)\mu}2\mu r^{-n-1} & \dfrac{(n^2+2n)\lambda+(n^2+2n-1)\mu}{(n+3)\lambda+(n+5)\mu}2\mu r^{n} & 2\mu(n-1)r^{n-2} \end{pmatrix}, \tag{11}$$

where n is the spherical harmonic degree.

There are two sets of toroidal solutions, one regular and one irregular, as formula (12):

$$\begin{pmatrix} y^{t}_{11}(r) & y^{t}_{12}(r) \\ y^{t}_{21}(r) & y^{t}_{22}(r) \end{pmatrix} = \begin{pmatrix} r^{n} & -r^{-(n+1)} \\ \mu(n-1)r^{n-1} & \mu(n+2)r^{-(n+2)} \end{pmatrix}. \tag{12}$$

We use the same path of integration as the one discussed in Wang *et al.* (2006), but based on the spherical earth model (Fig. 1), the formula can be written as

$$\boldsymbol{y}_j(r)\big|_{r=r_s^+} - \boldsymbol{y}_j(r)\big|_{r=r_s^-} = \boldsymbol{s}_j, \qquad j = 1,\ 2,\ 3,\ 4, \tag{13}$$

where $\boldsymbol{s}$ is seismic source function and j represents one of four independent sources (strike-slip, dip-slip, horizontal tensile and vertical tensile sources), defined by Takeuchi & Saito (1972).

The boundary conditions take the following form:

$$y_2(r)|_{r=R} = y_4(r)|_{r=R} = 0. \tag{14}$$

Then, by the four source functions and the path of integration as in Wang *et al.* (2006), we get the following equations for the spheroidal solutions (15) and toroidal solutions (16). We can obtain the coefficients $\beta_i (i = 1,\ 2,\ \ldots,\ 6)$ and $\beta^{t}_i (i = 1,\ 2,\ 3)$ analytically:

$$\begin{pmatrix} y_{21}(R) & y_{22}(R) & y_{23}(R) & y_{24}(R) & 0 & 0 \\ y_{41}(R) & y_{42}(R) & y_{43}(R) & y_{44}(R) & 0 & 0 \\ y_{11}(r_s^+) & y_{12}(r_s^+) & y_{13}(r_s^+) & y_{14}(r_s^+) & -y_{13}(r_s^-) & -y_{14}(r_s^-) \\ y_{21}(r_s^+) & y_{22}(r_s^+) & y_{23}(r_s^+) & y_{24}(r_s^+) & -y_{23}(r_s^-) & -y_{24}(r_s^-) \\ y_{31}(r_s^+) & y_{32}(r_s^+) & y_{33}(r_s^+) & y_{34}(r_s^+) & -y_{33}(r_s^-) & -y_{34}(r_s^-) \\ y_{41}(r_s^+) & y_{42}(r_s^+) & y_{43}(r_s^+) & y_{44}(r_s^+) & -y_{43}(r_s^-) & -y_{44}(r_s^-) \end{pmatrix} \begin{pmatrix} \beta_1 \\ \beta_2 \\ \beta_3 \\ \beta_4 \\ \beta_5 \\ \beta_6 \end{pmatrix} = \begin{pmatrix} 0 \\ 0 \\ s_1^{12}(r_s) \\ s_2^{12}(r_s) \\ s_3^{12}(r_s) \\ s_4^{12}(r_s) \end{pmatrix} \tag{15}$$

$$\begin{pmatrix} y^{t}_{21}(R) & y^{t}_{22}(R) & 0 \\ y^{t}_{11}(r_s^+) & y^{t}_{12}(r_s^+) & -y^{t}_{11}(r_s^-) \\ y^{t}_{21}(r_s^+) & y^{t}_{22}(r_s^+) & -y^{t}_{21}(r_s^-) \end{pmatrix} \begin{pmatrix} \beta^{t}_1 \\ \beta^{t}_2 \\ \beta^{t}_3 \end{pmatrix} = \begin{pmatrix} 0 \\ s_1^{t,12}(r_s) \\ s_2^{t,12}(r_s) \end{pmatrix}, \tag{16}$$

where R is the radius of the Earth and $r_s = (R - d_s)/R$ denotes the normalized radial distance of the source.

Using the regular foundation solutions and the constant values β of the spheroidal and toroidal parts, we can get the deformation factors of displacement and strain changes:

$$y_j(r) = \sum_{i=1}^{4} \beta_i y_{ji}(r), \qquad j = 1,\ 2,\ 3,\ 4. \tag{17}$$

In order to derive expressions for the internal co-seismic deformation at an arbitrary layer (h) inside the Earth, we apply two conditions to the regular solutions:

Table 1. Love numbers and Green's functions caused by four independent point sources.

Love numbers:
$h_n^{ij} = y_1^{n,ij}(r) \cdot R^2$
$l_n^{ij} = y_3^{n,ij}(r) \cdot R^2$ $\quad ij = 12, 32, 22, 33$ $\quad \kappa = \frac{\lambda}{\lambda+2\mu}$
$l_n^{t,n,ij} = y_1^{t,n,ij}(r) \cdot R^2$
$ij = 12$—Strike-Slip, $ij = 32$—Dip-Slip, $ij = 22$—Horizontal tensile, and $ij = 33$—Vertical tensile

GF	Strike-slip	Dip-slip	Horizontal tensile	Vertical tensile
u_r	$2\sum_{n=2}^{\infty} h_{n2}^{12} P_n^2(\cos\theta)\sin 2\phi$	$-2\sum_{n=1}^{\infty} h_{n1}^{32} P_n^1(\cos\theta)\sin\phi$	$\sum_{n=0}^{\infty} h_{n0}^{22} P_n(\cos\theta)$	$\sum_{n=0}^{\infty} h_{n0}^{33} P_n(\cos\theta)$
u_θ	$2\sum_{n=2}^{\infty} [l_{n2}^{12} \frac{\partial P_n^2(\cos\theta)}{\partial\theta} + 2l_{n2}^{t,12} \frac{P_n^2(\cos\theta)}{\sin\theta}]\sin 2\phi$	$-2\sum_{n=1}^{\infty} [l_{n1}^{32} \frac{\partial P_n^1(\cos\theta)}{\partial\theta} - l_{n1}^{t,32} \frac{P_n^1(\cos\theta)}{\sin\theta}]\sin\phi$	$\sum_{n=0}^{\infty} l_{n0}^{22} \frac{\partial P_n(\cos\theta)}{\partial\theta}$	$\sum_{n=0}^{\infty} l_{n0}^{33} \frac{\partial P_n(\cos\theta)}{\partial\theta}$
u_ϕ	$2\sum_{n=2}^{\infty} [2l_{n2}^{12} \frac{P_n^2(\cos\theta)}{\sin\theta} + l_{n2}^{t,12} \frac{\partial P_n^2(\cos\theta)}{\partial\theta}]\cos 2\phi$	$-2\sum_{n=1}^{\infty} [l_{n1}^{32} \frac{P_n^1(\cos\theta)}{\sin\theta} + l_{n1}^{t,32} \frac{\partial P_n^1(\cos\theta)}{\partial\theta}]\cos\phi$	0	0
e_{rr}	$2\kappa\sum_{n=2}^{\infty} (2h_{n2}^{12} - n(n+1)l_{n2}^{12}) P_n^2(\cos\theta)\sin 2\phi$	$2\kappa\sum_{n=1}^{\infty} (2h_{n1}^{32} - n(n+1)l_{n1}^{32}) P_n^1(\cos\theta)\sin\phi$	$\kappa\sum_{n=0}^{\infty} [-h_{n0}^{22} + n(n+1)l_{n0}^{22}] P_n(\cos\theta)$	$\kappa\sum_{n=0}^{\infty} [-h_{n0}^{33} + n(n+1)l_{n0}^{33}] P_n(\cos\theta)$
$e_{\theta\theta}$	$2\sum_{n=2}^{\infty} [\begin{matrix} -l_{n2}^{12} \frac{d^2 P_n^2(\cos\theta)}{d\theta^2} - h_{n2}^{12} P_n^2(\cos\theta) \\ -2l_{n2}^{t,12} (\frac{1}{\sin\theta} \frac{dP_n^2(\cos\theta)}{d\theta} - \frac{\cos\theta}{\sin^2\theta} P_n^2(\cos\theta)) \end{matrix}]\sin 2\phi$	$2\sum_{n=1}^{\infty} [\begin{matrix} -l_{n1}^{32} \frac{d^2 P_n^1(\cos\theta)}{d\theta^2} - h_{n1}^{32} P_n^1(\cos\theta) \\ -l_{n1}^{t,32} (\frac{1}{\sin\theta} \frac{dP_n^1(\cos\theta)}{d\theta} - \frac{\cos\theta}{\sin^2\theta} P_n^1(\cos\theta)) \end{matrix}]\sin\phi$	$\sum_{n=0}^{\infty} [l_{n0}^{22} \frac{d^2 P_n(\cos\theta)}{d\theta^2} + h_{n0}^{22} P_n(\cos\theta)]$	$\sum_{n=0}^{\infty} [l_{n0}^{33} \frac{d^2 P_n(\cos\theta)}{d\theta^2} + h_{n0}^{33} P_n(\cos\theta)]$
$e_{\phi\phi}$	$2\sum_{n=2}^{\infty} \{\begin{matrix} \frac{l_{n2}^{12}}{\sin\theta} (\frac{4P_n^2(\cos\theta)}{\sin\theta} - \cos\theta \frac{dP_n^2(\cos\theta)}{d\theta}) \\ -h_{n2}^{12} P_n^2(\cos\theta) \\ +2\frac{l_{n2}^{t,12}}{\sin\theta} (\frac{dP_n^2(\cos\theta)}{d\theta} - \cot\theta P_n^2(\cos\theta)) \end{matrix}\}\sin 2\phi$	$2\sum_{n=1}^{\infty} \{\begin{matrix} \frac{l_{n1}^{32}}{\sin\theta} (\frac{P_n^1(\cos\theta)}{\sin\theta} - \cos\theta \frac{dP_n^1(\cos\theta)}{d\theta}) \\ -h_{n1}^{32} P_n^1(\cos\theta) \\ +\frac{l_{n1}^{t,32}}{\sin\theta} (\frac{dP_n^1(\cos\theta)}{d\theta} - \cot\theta P_n^1(\cos\theta)) \end{matrix}\}\sin\phi$	$\sum_{n=0}^{\infty} [\begin{matrix} \cot\theta l_{n0}^{22} \frac{dP_n(\cos\theta)}{d\theta} \\ +h_{n0}^{22} P_n(\cos\theta) \end{matrix}]$	$\sum_{n=0}^{\infty} [\begin{matrix} \cot\theta l_{n0}^{33} \frac{dP_n(\cos\theta)}{d\theta} \\ +h_{n0}^{33} P_n(\cos\theta) \end{matrix}]$
$e_{\theta\phi}$	$2\sum_{n=2}^{\infty} \{\begin{matrix} \frac{4l_{n2}^{12}}{\sin\theta} (-\frac{dP_n^2(\cos\theta)}{d\theta} + \cot\theta P_n^2(\cos\theta)) \\ +l_{n2}^{t,12} (\cot\theta \frac{dP_n^2(\cos\theta)}{d\theta} - \frac{4P_n^2(\cos\theta)}{\sin^2\theta} \\ - \frac{d^2 P_n^2(\cos\theta)}{d\theta^2}) \end{matrix}\}\cos 2\phi$	$2\sum_{n=1}^{\infty} \{\begin{matrix} \frac{2l_{n1}^{32}}{\sin\theta} (-\frac{dP_n^1(\cos\theta)}{d\theta} + \cot\theta P_n^1(\cos\theta)) \\ +l_{n1}^{t,32} (\cot\theta \frac{dP_n^1(\cos\theta)}{d\theta} - \frac{P_n^1(\cos\theta)}{\sin^2\theta} \\ - \frac{d^2 P_n^1(\cos\theta)}{d\theta^2}) \end{matrix}\}\cos\phi$	0	0

(1) When $h < d_s$, the internal surface is located between the surface and the seismic source. The y-variables take the following form:

$$\begin{pmatrix} y_1 \\ y_3 \end{pmatrix} = \begin{pmatrix} y_{11}(r) & y_{12}(r) & y_{13}(r) & y_{14}(r) \\ y_{31}(r) & y_{32}(r) & y_{33}(r) & y_{34}(r) \end{pmatrix} \begin{pmatrix} \beta_1 \\ \beta_2 \\ \beta_3 \\ \beta_4 \end{pmatrix}$$

$$y_1^{\mathrm{t}} = \begin{pmatrix} y_{11}^{\mathrm{t}}(r) & y_{12}^{\mathrm{t}}(r) \end{pmatrix} \begin{pmatrix} \beta_1^{\mathrm{t}} \\ \beta_2^t \end{pmatrix} \tag{18}$$

(2) When $h > d_s$, the internal surface is located between the seismic source and the centre of the Earth. The y-variables take the following form:

$$\begin{pmatrix} y_1 \\ y_3 \end{pmatrix} = \begin{pmatrix} y_{13}(r) & y_{14}(r) \\ y_{33}(r) & y_{34}(r) \end{pmatrix} \begin{pmatrix} \beta_5 \\ \beta_6 \end{pmatrix}$$

$$y_1^{\mathrm{t}} = y_{11}^t(r)\beta_3^{\mathrm{t}}. \tag{19}$$

By these y-variables at different depth, we can get the Love numbers and Green's functions (GF) for displacement and strain changes (Table 1) inside the Earth.

With the new set of internal Love number formulae, we can get the internal Green's functions for displacement (u_r, u_θ, u_ϕ) and strain ($e_{rr}, e_{\theta\theta}, e_{\phi\phi}, e_{\theta\phi}$) changes generated by four independent sources in a homogeneous spherical Earth. Usually, a finite fault model can be divided into many subfaults. When the subfaults are small enough, they can be approximated as point sources (Beresnev & Atkinson 1997, 1998) and summed up the individual contributions to get the total deformation of the finite fault. That is to say, any finite fault can be combined with the four independent point sources by its strike angle, dip angle, rake angle, etc. Then, these Green's functions can be applied to arbitrary point sources and finite fault models. Though our approach is based on a homogeneous spherical model, it represents a step forward for the application of dislocation theory to this internal deformation puzzle in multiple reference frames and Earth scenarios.

Based on eqs (18) and (19) and Table 1, we can calculate the internal deformation inside the Earth at an arbitrary depth with the exception of the source point, which, according to our parametrization, is a discontinuous point. These calculations will provide insight into the internal deformation of a complex, layered earth model.

2.2 Harmonic degree effect on numerical convergence

Due to the complexity and computing time of spherical dislocation theory, Sun *et al.* (2009) applied a constraint of $n_{\max} = 10 \cdot R/d_s$ to expedite the computing process while maintaining the desired level of precision. We apply the same truncation procedure, but our approach

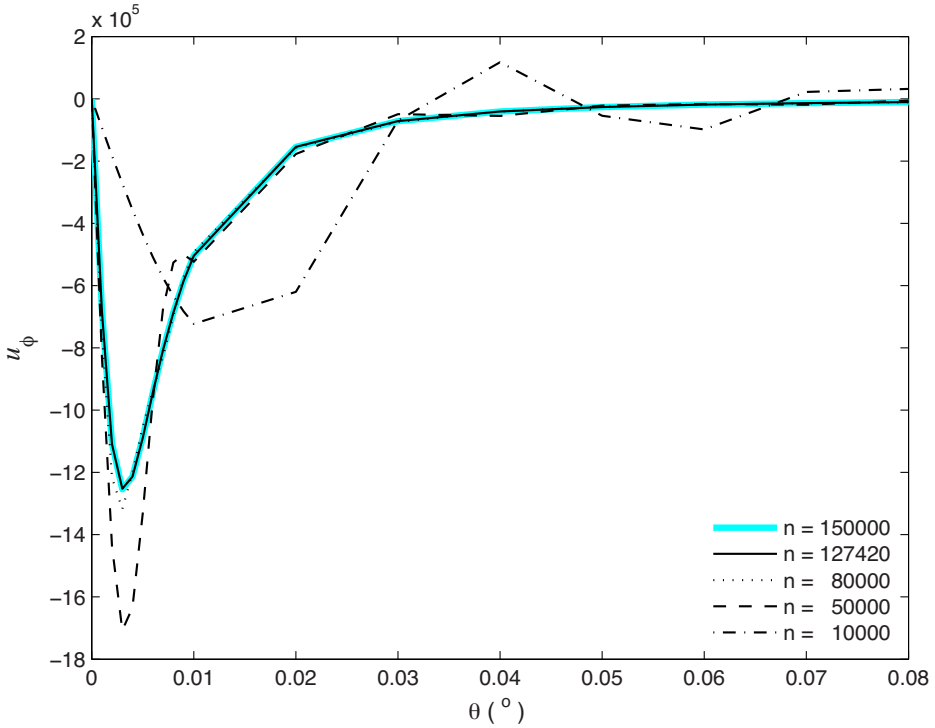

Figure 2. Comparison of Green's functions at 19.5 km with different calculated spherical harmonic degrees (n) caused by a strike-slip point source ($d_s = 20$ km, $\mathrm{UdS}/R^2 = 1$).

also allows us to quickly calculate n values that are larger than $n_{\max}$:

$$n > n_{\max} = \frac{10\,R}{|d_s - h_n|}. \tag{20}$$

The degree n should be truncated to at least $n_{\max}$ to avoid the non-convergence. For $h_n = 19.5$ km and $d_s = 20.0$ km, we need to calculate at least $n_{\max} = 127\,420$, which exceeded the number of available calculated degrees in the surface deformation calculation of Sun *et al.* (2009). For the homogeneous spherical earth model, Takagi & Okubo (2017) used the foundation solutions of Love (1911) and introduced the asymptotic solutions to solve the non-convergence problem near the source. For the half-space earth model, Okada (1992) presented the analytical solutions for the internal deformation calculation. Our formulae resolve any convergence issue in the spherical earth model without requiring additional numerical techniques.

In order to validate the stabilization of the Green's functions with the spherical harmonic degree, we calculate the internal horizontal displacement at a distance of 19.5 km from a strike-slip source with a depth of 20 km. In this case, $n_{\max} = 127\,420$. Theoretically, it is non-convergent when n is truncated less than $n_{\max}$. In Fig. 2, we can see that the results are non-convergent for $n = 10\,000$. When $n = 50\,000$, though the results are convergent, the real values are inaccurate. While the results of $n = 80\,000$ are close to those of $n = 127\,420$, the values are still not accurate. Conversely, the results for $n = 127\,420$ and $n = 150\,000$ are identical and converging; when $n \geq n_{\max}$, all calculations are accurate. In addition, our foundation solutions are analytical, we do not need to consider the computing time for the high degrees.

3 COMPUTING RESULTS

3.1 Internal co-seismic deformation caused by point sources

Using the aforementioned model, we calculated the internal displacement (Fig. 3) and strain changes (Fig. 4) caused by the four independent point sources ($d_s = 20$ km). The point sources are normalized by a factor of $\mathrm{UdS}/R^2 = 1$. In order to characterize the deformation at different depths, we divide our inner deformation results into two parts: those above ($h = 0$ km, $h = 2$ km, $h = 12$ km) and below ($h = 28$ km, $h = 40$ km) the source. The surface deformation occurs at $h = 0$ km. Layers $h = 12$ km and $h = 28$ km are equidistant from the source, which has a depth of 20 km.

From Fig. 3, the displacements inside the Earth are larger than those on the surface ($h = 0$ km). The amplitudes of displacements at layer $h = 12$ km are more than twice as large as the surface. For the deformation at equidistant layers from the source, such as $h = 12$ km and $h = 28$ km, the displacements are not identical though sometimes their signs are the same. For the strike-slip, horizontal tensile and vertical tensile sources, the sign of the radial displacement (u_r) changes depending on whether the deformation is above or below the source; however,

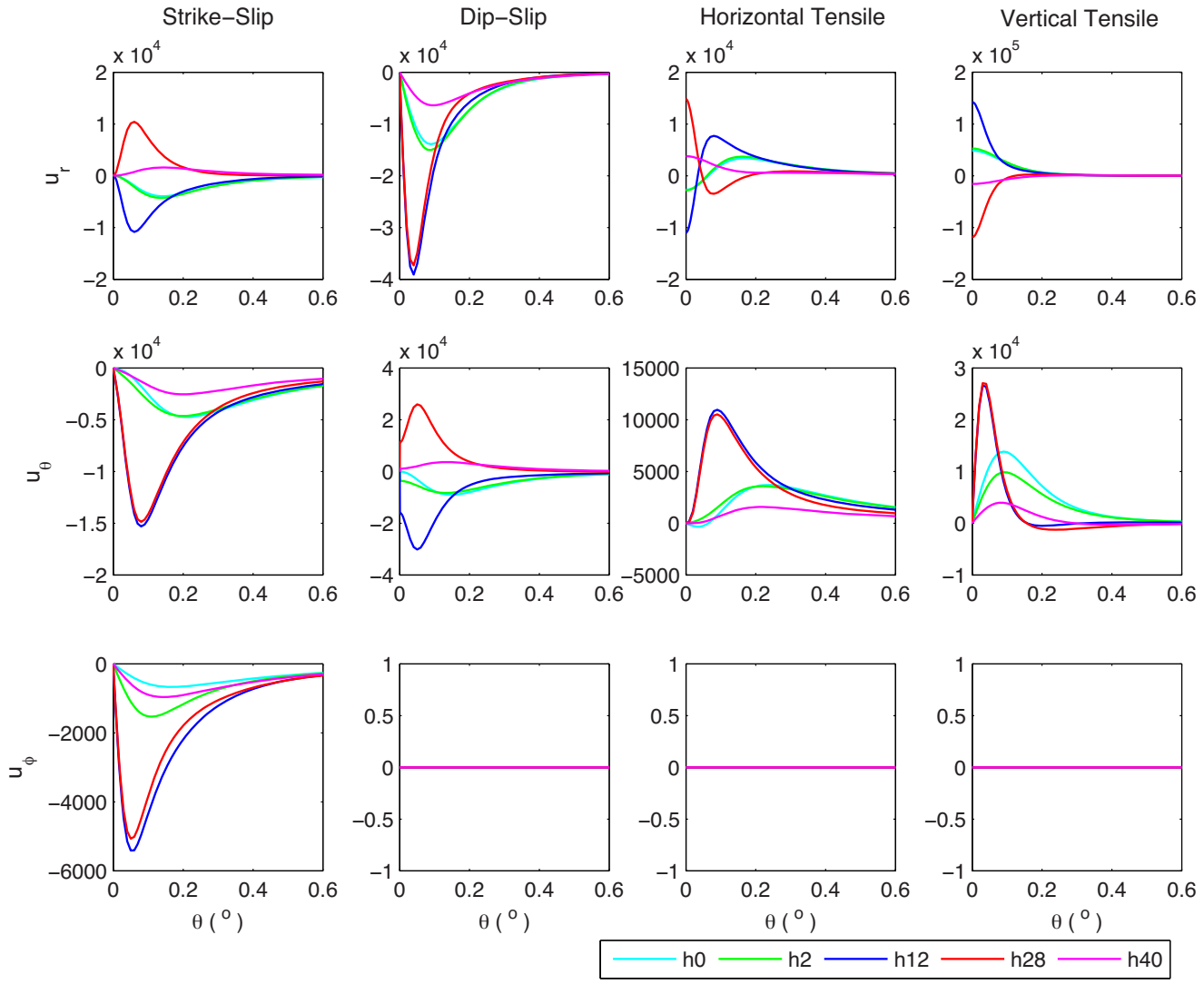

Figure 3. Internal displacement (u_r, u_θ, u_ϕ) caused by four point sources ($d_s = 20$ km, UdS/$R^2 = 1$) at different depths (0, 2, 12, 28 and 40 km) in the Earth.

the sign for the horizontal displacements (u_θ, u_ϕ) stays the same regardless of the depth. This trend is reversed for the dip-slip source, which has similarly signed radial displacements and oppositely signed horizontal displacements.

The strain magnitudes fall off rapidly with increased distance from the source. While the sign of the strain appears to be independent of the study location for the strike-slip, horizontal tensile and vertical tensile sources, the sign of the strain magnitude for the dip-slip source appears to depend on the study location. Remarkably, the amplitudes of the deformation at the two layers that are equidistant from the source ($h = 12$ km and $h = 28$ km) are not identical; there are minor differences between the two.

As shown in Figs 3 and 4, the internal deformation is much larger than that expressed at the surface. The magnitude of the deformation is highest close to the source, and decreases with increased distance from the source.

3.2 Co-seismic strain changes at an internal sphere

In order to study the internal deformation properties at an internal sphere, we placed the point sources at the north pole (Sun & Okubo 1993) and analysed the deformation that occurred within the $h = 40$ km layer in a quadrant pattern.

For the strike-slip source, components e_{rr} and $e_{\phi\phi}$ rise in quadrants 1 and 3 and sink down in quadrants 2 and 4; the reverse is true for components $e_{\theta\theta}$ and $e_{\theta\phi}$(Fig. 5). For the dip-slip source, the strain component e_{rr} sinks down when the latitude is positive, but rises when the latitude is negative; the reverse is true for components $e_{\theta\theta}$, $e_{\phi\phi}$, $e_{\theta\phi}$ (Fig. 6). For the horizontal and vertical tensile sources, the strain properties are the same in all four quadrants (Figs 7 and 8). The strain component $e_{\theta\phi}$ for the tensile sources is equal to zero.

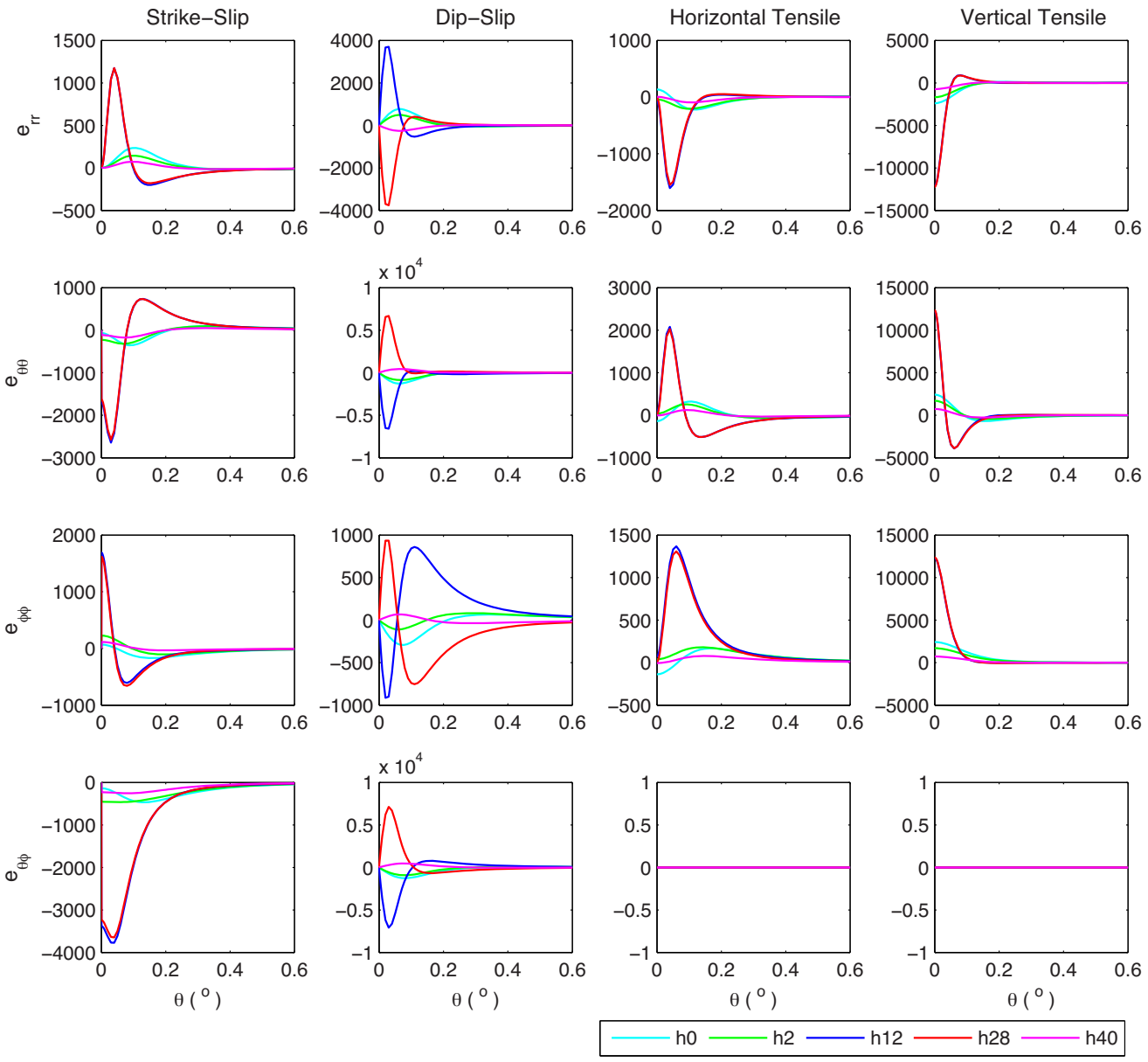

Figure 4. Internal strain (e_{rr}, $e_{\theta\theta}$, $e_{\phi\phi}$, $e_{\theta\phi}$) changes caused by four point sources ($d_s = 20$ km, UdS/$R^2 = 1$) at different depths (0, 2, 12, 28 and 40 km) in the Earth.

3.3 Internal co-seismic deformations at radial section plane

In Fig. 9, we compare our internal deformation depth dependency results for a spherical model (specifically, the radial section plane) with those of the half-space model shown in Okada (1992). We calculated the internal displacement and strain changes caused by four independent sources from $h = 0$ km to $h = 60$ km. Because the source is defined as a discontinuity in the SNREI Earth, we do not present the results in the immediate vicinity of the point source. The results in Fig. 9 were calculated at an epicentral angular distance of $\theta = 0.1^\circ$. For the displacements u_θ, u_ϕ and strain changes e_{rr}, $e_{\theta\theta}$, $e_{\phi\phi}$, $e_{\theta\phi}$ caused by strike-slip and tensile sources, the deformations are similar both above and below the source, even if the magnitude of the deformation varies slightly at layers equidistant from the source. Conversely, the strike-slip and tensile source displacements u_r and the dip-slip displacements u_θ, u_ϕ and strain changes e_{rr}, $e_{\theta\theta}$, $e_{\phi\phi}$, $e_{\theta\phi}$ appear to have point symmetry.

The magnitudes of the strain components decay more rapidly than those of the displacement components with increased distance from the source. This phenomenon depends on the definition of strain. An internal deformation model should be based on a spherical Earth in order to account for the curvature effect. The effect of the layered structures on deformation is larger than the curvature (Pollitz 1996; Sun & Okubo 2002; Melini *et al.* 2008; Dong *et al.* 2014). Dong *et al.* (2014) found that the effect of the curvature on the displacements is $\leq$5 per cent. In order to fully account for the curvature and layered structure effects in our understanding of internal deformation, we wll apply our calculations to a more complex layered spherical earth model next.

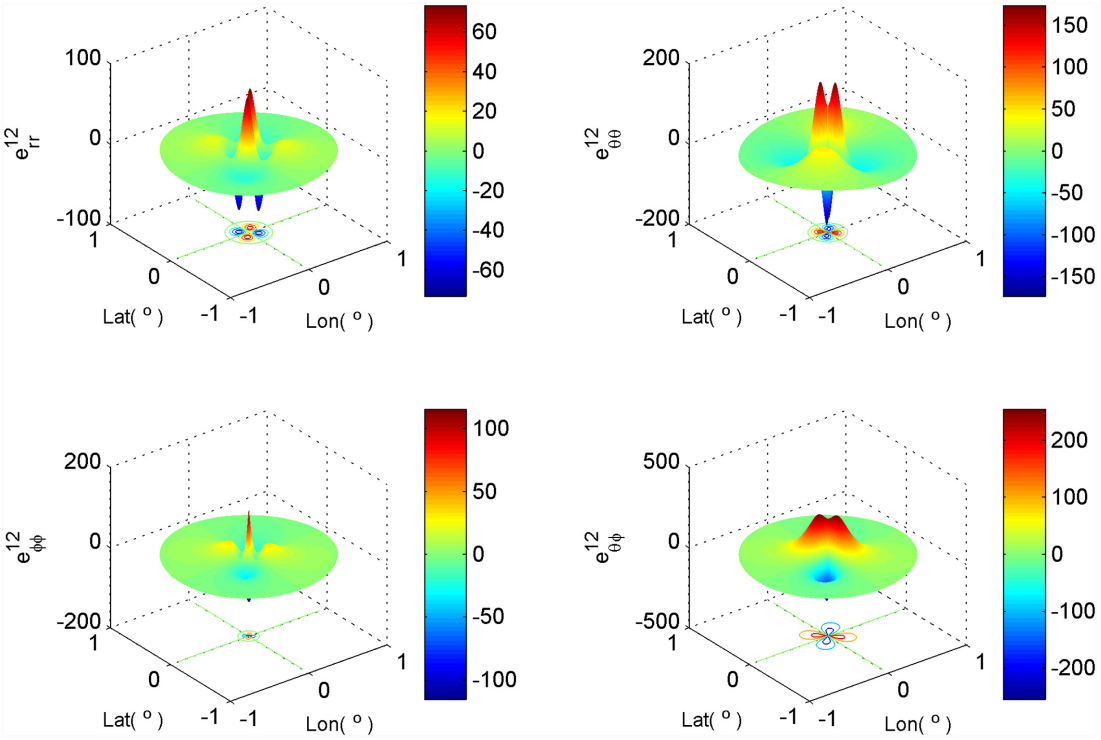

Figure 5. Strain changes (e_{rr}, $e_{\theta\theta}$, $e_{\phi\phi}$, $e_{\theta\phi}$) in a quadrant pattern at $h = 40$ km caused by a strike-slip source ($d_s = 20$ km, UdS/$R^2 = 1$) located at the north pole.

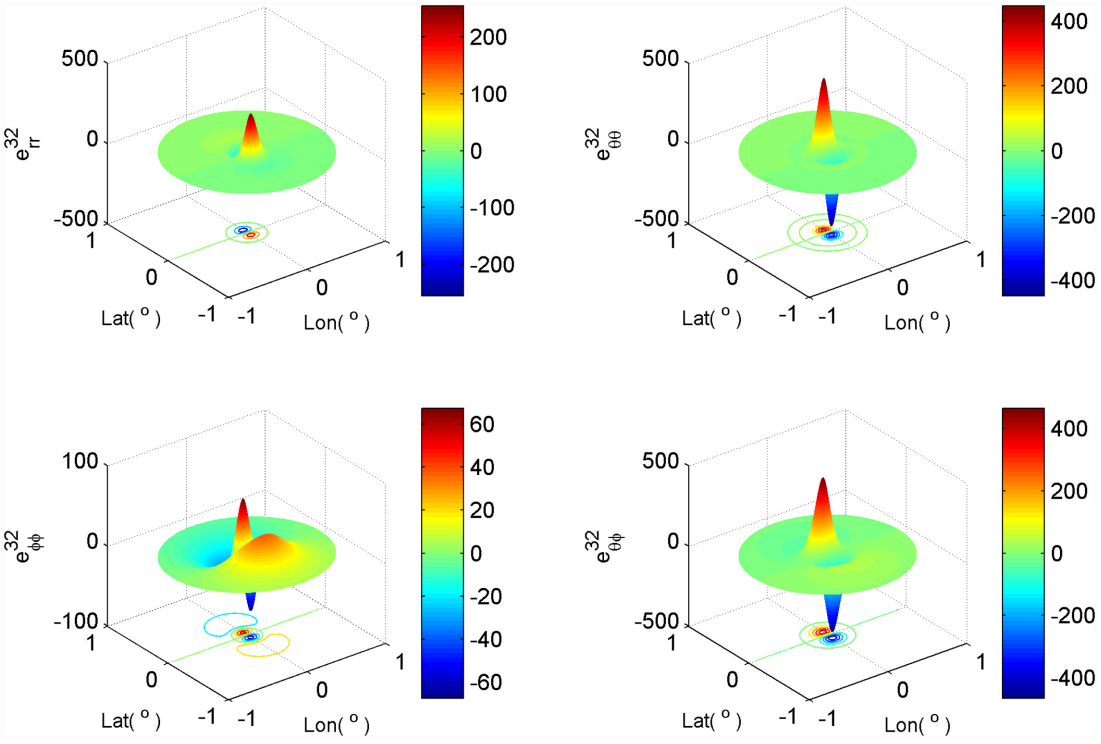

Figure 6. Similar to Fig. 5, but for dip-slip source.

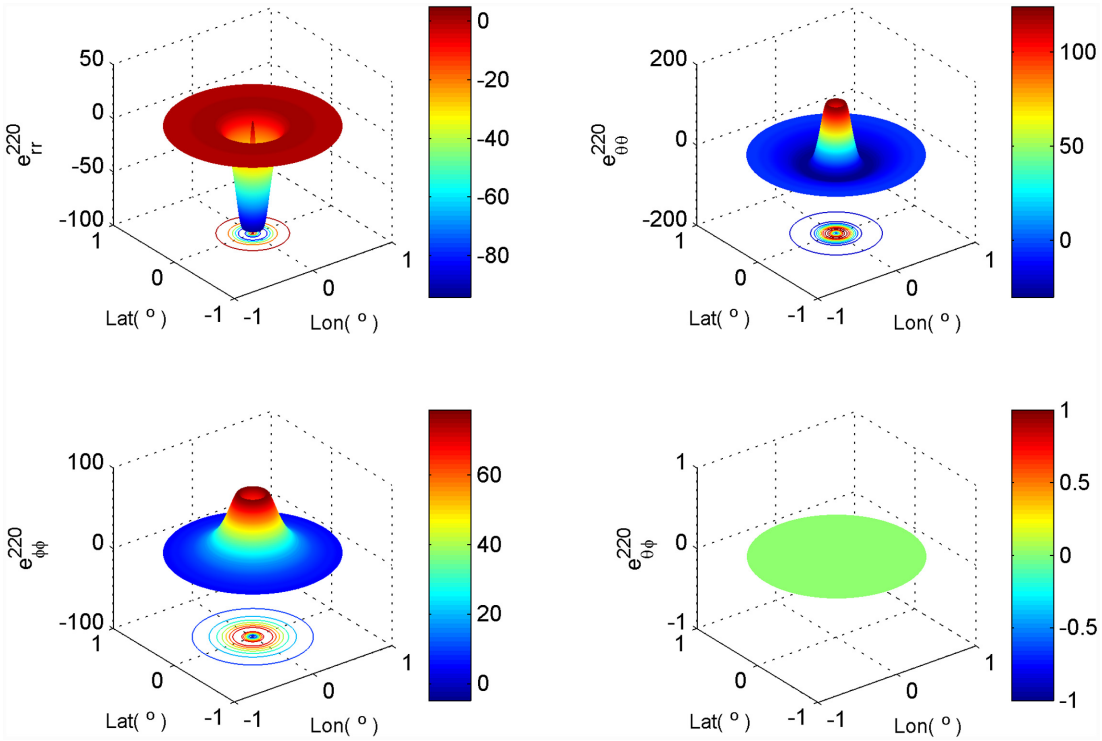

Figure 7. Similar to Fig. 5, but for horizontal tensile source.

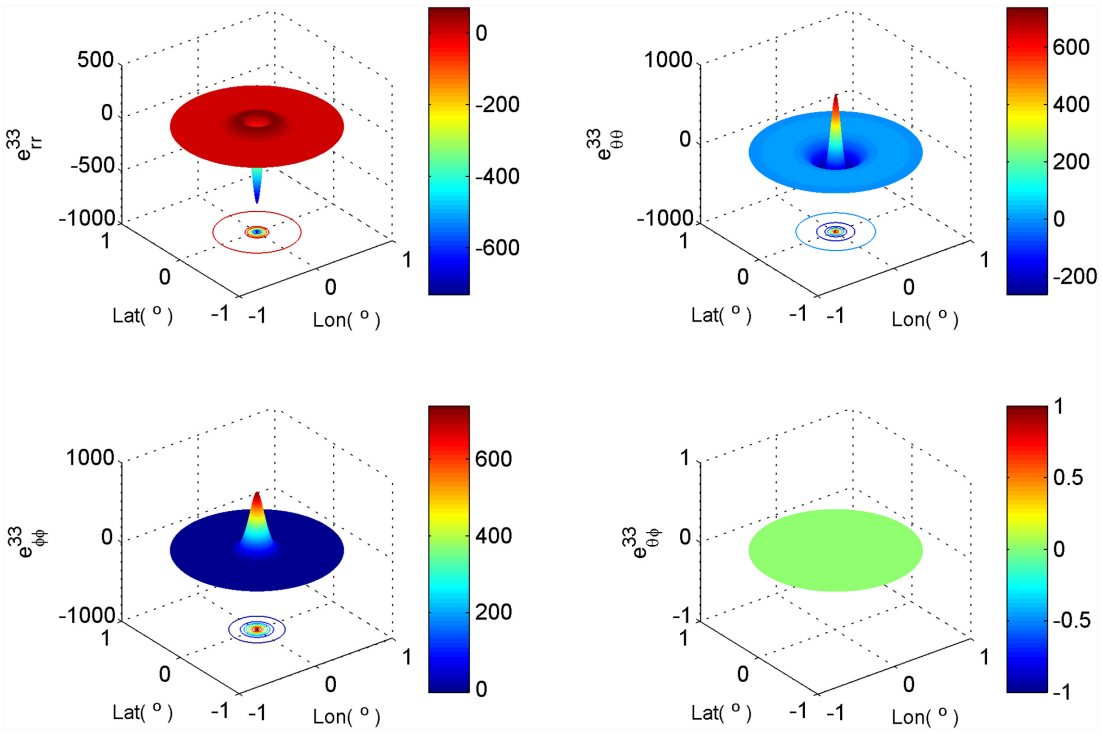

Figure 8. Similar to Fig. 5, but for vertical tensile source.

4 INTERNAL DEFORMATIONS IN SPHERICAL AND HALF-SPACE MODELS

Many studies that invoke the work of Okada (1985, 1992) operate under the assumption that the curvature effect is negligible. However, as shown in Fig. 10, our results indicate that the curvature of the Earth is non-trivial when it comes to internal co-seismic deformation, especially for far-field deformation.

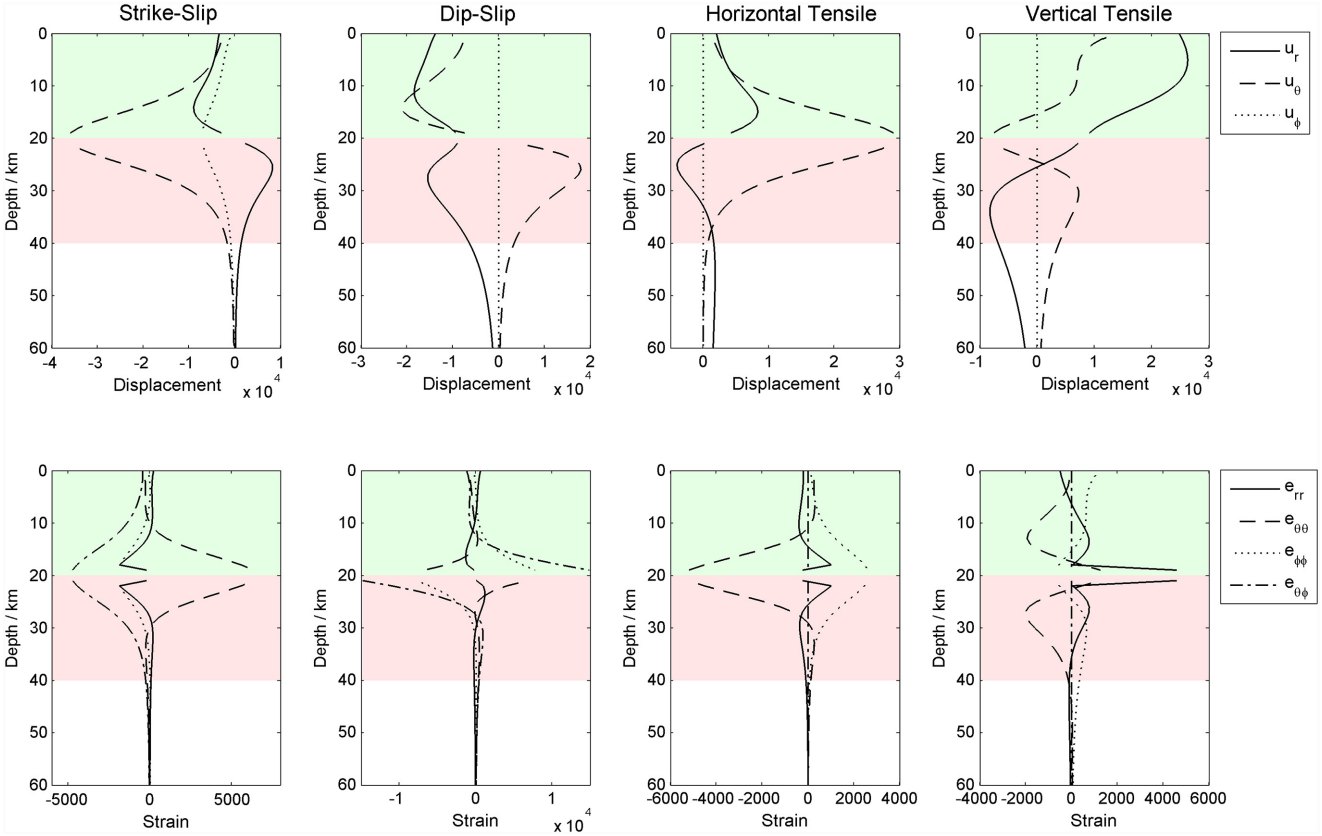

Figure 9. Radial section plane of internal displacement (u_r, u_θ, u_ϕ) and strain ($e_{rr}, e_{\theta\theta}, e_{\phi\phi}, e_{\theta\phi}$) changes caused by four point sources ($d_s = 20$ km, $\mathrm{UdS}/R^2 = 1$). The green part represents the area between the surface ($h = 0$ km) and the seismic source ($h = 20$ km). The red part represents the area between the seismic source ($h = 20$ km) and a lower layer ($h = 40$ km).

In Fig. 10, we compare the internal radial displacement (u_r) values for a strike-slip source ($d_s = 20$ km) for our spherical model and a half-space model. For both models, the point sources are normalized by a factor of $\mathrm{UdS}/R^2 = 1$. The relation between distance from the source (l) and epicentral angle (θ) is $l \approx 20000 \cdot \theta/180$. Our results include both near-field ($l_{\theta=0.1^\circ} \approx 11.1$ km) and far-field ($l_{\theta=16^\circ} \approx 1778$ km) displacements to show the curvature effect (Fig. 10). Because the values at shallow depth (0–60 km) and deep depth (1000–3000 km) have a great difference by seven orders of magnitude in near-field area, we plot the internal displacements with three subfigures in Figs 10(a)–(c). At shallow depths, the curvature effect is small and the curves almost overlap each other (Fig. 10a). The effects increase with depth, which can reach 30 per cent at $h = 1000$ km. For the far-field deformation at $l_{\theta=16^\circ} \approx 1778$ km, the internal displacements decay slowly with distance from the source (Fig. 10d). The maximum internal displacement value is five times larger than the surface deformation in the spherical model, whereas the maximum internal displacement is only twice that observed at the surface in the half-space model. The curvature effect is obviously large at every depth; on the surface, it can be as high as 77 per cent. It is important to study the internal deformation of a spherical earth model because it provides us with insight into how seemingly negligible effects, such as the curvature, affect internal deformation both in the near-field and in the far-field.

5 CONCLUSIONS

In this study, we present a new set of analytical foundation solutions that allow us to calculate the internal displacement (u_r, u_θ, u_ϕ) and strain ($e_{rr}, e_{\theta\theta}, e_{\phi\phi}, e_{\theta\phi}$) changes caused by four independent sources (strike-slip, dip-slip, horizontal tensile and vertical tensile) in a homogeneous spherical model. Although the formulae include the spherical harmonic degree, they are analytical and they can be calculated up to any degree directly without employing any additional numerical techniques.

From our calculation, we can see that the internal deformations are larger than those apparent at the surface. The signs of radial displacements (u_r) caused by the strike-slip and tensile sources are dependent upon the layer location with respect to the source, while the signs of the Green's function components ($u_\theta, u_\phi, e_{rr}, e_{\theta\theta}, e_{\phi\phi}, e_{\theta\phi}$) appear to be the same throughout our model; this trend is reversed for the dip-slip source.

Looking at internal deformation at a sphere at $h = 40$ km, the deformation pattern for a strike-slip source consisted of components of e_{rr} and $e_{\phi\phi}$ rising in quadrants 1 and 3 and sinking down in quadrants 2 and 4, while the components of $e_{\theta\theta}$ and $e_{\theta\phi}$ behave in the opposite fashion. For the dip-slip source, the strain component e_{rr} sinks down when the latitude is positive, but rises when the latitude is negative;

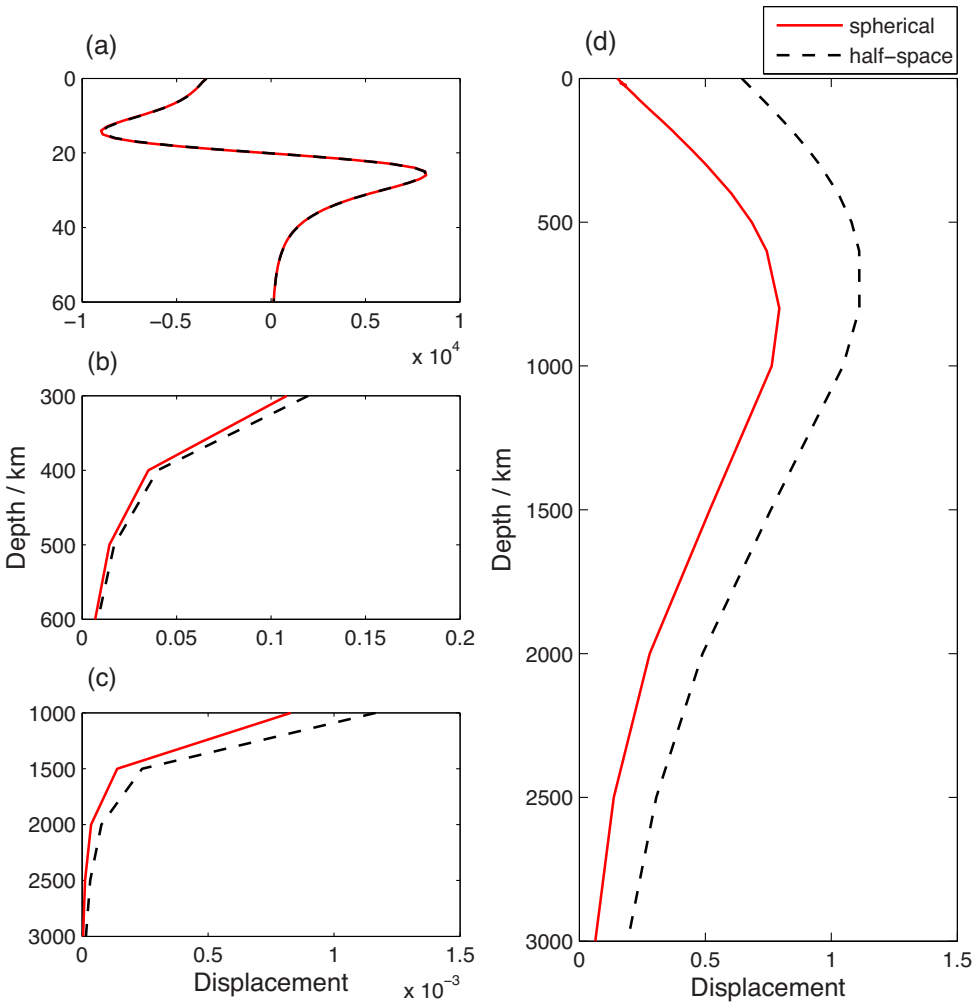

Figure 10. Radial section plane showing internal radial displacement (u_r) at $\theta = 0.1^\circ$ (a–c) and $\theta = 16^\circ$ (d) caused by a strike-slip source ($d_s = 20$ km, $\mathrm{UdS}/R^2 = 1$) in a spherical model and a half-space model.

the opposite is true for components $e_{\theta\theta}, e_{\phi\phi}, e_{\theta\phi}$. For the tensile sources, the properties are the same in all four quadrants, and the strain component $e_{\theta\phi}$ for tensile sources is equal to zero.

The internal deformation components $u_\theta, u_\phi, e_{rr}, e_{\theta\theta}, e_{\phi\phi}, e_{\theta\phi}$ caused by strike-slip and tensile sources at a radial section plane ($\theta = 0.1^\circ$) appear symmetric at an equal distance above and below the source, but the amplitudes of the deformation are slightly different. The strike-slip and tensile source radial displacements u_r and the dip-slip displacements $u_\theta, u_\phi$and strain changes $e_{rr}, e_{\theta\theta}, e_{\phi\phi}, e_{\theta\phi}$ all seem to exhibit point symmetry, but also have slightly different deformation amplitudes.

As shown by the difference between the internal radial displacements for the spherical and half-space models, it is not accurate to neglect the curvature effect of the Earth. In the near-field, the curvature effect at shallow depths is small, but it increases with depth. At $h = 1000$ km, the curvature effect is as high as 30 per cent at $l_{\theta=0.1^\circ} \approx 11.1$ km. In the far-field, the curvature effect is large at every depth. Especially for that on the surface, it can reach 77 per cent at $l_{\theta=16^\circ} \approx 1778$ km.

The study of internal deformation can improve the dislocation theory. Moreover, it is important for the study of accumulation and distribution of stress. Comparing with the transferred stress in a global viscoelastic model (Casarotti *et al.* 2001), we can further discuss the focal mechanism in the seismic cycle. Our future work will involve applying these calculations to a radially stratified spherical earth model and making our code, which calculates the internal deformation of point sources and involves a generalized finite fault model, available for public use.

ACKNOWLEDGEMENTS

We thank the two referees for thoughtful reviews and comments that helped to improve the manuscript. This study was supported financially by the National Natural Science Foundation of China (Nos. 41604067, 41974093, 41331066 and 41774088), the Basic Research Fund of Chinese Academy of Surveying and Mapping (No. AR 1906), the special project of high-resolution Earth observation system (42-Y20A09-9001-17/18) and the Key Research Program of Frontier Sciences Chinese Academy of Sciences (QYZDY-SSW-SYS003).

DATA AVAILABILITY

All the data of displacement and strain changes caused by four independent point sources are calculated by our formulae and Okada's (1992).

REFERENCES

Alterman, Z., Jarosch, H. & Pekeris, C.L., 1959. Oscillation of the Earth, *Proc. R. Soc. Lond,* **A252,** 80–95.

Barbot, S. & Fialko, Y., 2010a. Fourier-domain Green's function for an elastic semi-infinite solid under gravity, with applications to earthquake and volcano deformation, *Geophys. J. Int.,* **182,** 568–582.

Barbot, S. & Fialko, Y., 2010b. A unified continuum representation of post-seismic relaxation mechanisms: semi-analytic models of afterslip, poroelastic rebound and viscoelastic flow, *Geophys. J. Int.,* **182,** 1124–1140.

Ben-Menahem, A. & Singh, S., 1968. Eigenvector expansions of Green's dyads with applications to geophysical theory, *Geophys. J. R. astr. Soc.,* **16,** 417–452.

Ben-Menahem, A., Singh, S. & Solomon, F., 1969. Static deformation of a spherical earth model by internal dislocations, *Bull. seism. Soc. Am.,* **59,** 813–853.

Ben-Menahem, A., Singh, S. & Solomon, F., 1970. Deformation of a homogeneous Earth model by finite dislocations, *Rev. Geophys. Space Phys.,* **8,** 591–632.

Beresnev, I.A. & Atkinson, G.M., 1997. Modeling finite-fault radiation from the ω^n spectrum, *Bull. seism. Soc. Am.,* **87**(1), 67–84.

Beresnev, I.A. & Atkinson, G.M., 1998. FINSIM—a FORTRAN program for simulating stochastic acceleration time histories from finite faults, *Seismol. Res. Lett.,* **69**(1), 27–32.

Casarotti, E., Piersanti, A., Lucente, F.P. & Boschi, E., 2001. Global postseismic stress diffusion and fault interaction at long distances, *Earth planet. Sci. Lett.,* **191**(1–2), 75–84.

Dahlen, 1968. The normal modes of a rotating, elliptical Earth, *Geophys. J. R. astr. Soc.,* **16,** 329–367.

Dong, J., Sun, W., Zhou, X. & Wang, R., 2014. Effects of Earth's layered structure, gravity and curvature on coseismic deformation, *Geophys. J. Int.,* **199**(3), 1442–1451.

Dong, J., Sun, W., Zhou, X. & Wang, R., 2016. An analytical approach to estimate curvature effect of coseismic deformations, *Geophys. J. Int.,* **206,** 1327–1339.

Dong, J., Cambiotti, G., Wen, H.J., Sabadini, R. & Sun, W., 2021. Treatment of discontinuities inside Earth models: effects on computed coseismic deformations, *Earth Planet. Phys.,* **5**(1), 90–104.

Farrell, W.E., 1972. Deformation of the Earth by surface loads, *Rev. Geophys. Space Phys.,* **10**(3), 761–797.

Fu, G. & Sun, W., 2007. Effects of lateral inhomogeneity in a spherical Earth on gravity Earth tides, *J. geophys. Res.,* **112,** B06409, doi:10.1029/2006JB004512.

Jovanovich, D., Husseini, M. & Chinnery, M., 1974a. Elastic dislocations in a layered half-space—I. Basic theory and numerical methods, *Geophys. J. R. astr. Soc.,* **39,** 205–217.

Jovanovich, D., Husseini, M. & Chinnery, M., 1974b. Elastic dislocations in a layered half-space—II. The point source, *Geophys. J. R. astr. Soc.,* **39,** 219–239.

Longman, I.M., 1962. A Green's function for determining the deformation of the Earth under surface mass loads: 1. Theory, *J. geophys. Res.,* **67,** 845–850.

Longman, I.M., 1963. A Green's function for determining the deformation of the Earth under surface mass loads: 2. Computations and numerical results, *J. geophys. Res.,* **68,** 485–496.

Love, A., 1911. *Some Problem of Geodynamics,* Cambridge Univ. Press.

Ma, X. & Kusznir, N., 1992. 3-D subsurface displacement and strain fields for faults and fault arrays in a layered elastic half-space, *Geophys. J. Int.,* **111**(3), 542–558.

Ma, C. & Lee, J., 2009. Theoretical analysis of generalized loadings and image forces in a planar magnetoelectroelastic layered half-plane, *J. Mech. Phys. Solids,* **57,** 598–620.

Matsu'ura, M., Tanimoto, T. & Iwasaki, T., 1981. Quasi-static displacements due to faulting in a layered half-space with an intervenient viscoelastic layer, *J. Phys. Earth,* **29,** 23–54.

Melini, D., Cannelli, V., Piersanti, A. & Spada, G., 2008. Post-seismic rebound of a spherical Earth: new insights from the application of the Post–Widder inversion formula, *Geophys. J. Int.,* **174**(2), 672–695.

Okada, Y., 1985. Surface deformation due to shear and tensile faults in a half-space, *Bull. seism. Soc. Am.,* **75**(4), 1135–1154.

Okada, Y., 1992. Internal deformation due to shear and tensile faults in a half-space, *Bull. seism. Soc. Am.,* **82**(2), 1018–1040.

Okubo, S., 1992. Gravity and potential changes due to shear and tensile faults in a half-space, *J. geophys. Res.,* **97**(B5), 7137–7144.

Pan, E., 1989a. Static response of a transversely isotropic and layered half-space to general surface loads, *Phys. Earth planet. Inter.,* **54,** 353–363.

Pan, E., 2019. Green's functions for geophysics: a review, *Rep. Prog. Phys.,* **82,** 106801, doi:10.1088/1361-6633/ab1877.

Pan, E., Yuan, J., Chen, W. & Griffith, W., 2014. Elastic deformation due to polygonal dislocations in a transversely isotropic half-space, *Bull. seism. Soc. Am.,* **104**(6), 2698–2716.

Piersanti, A., Spada, G., Sabadini, R. & Bonafede, M., 1995. Global postseismic deformation, *Geophys. J. Int.,* **120,** 544–566.

Piersanti, A., Spada, G. & Sabadini, R., 1997. Global postseismic rebound of a viscoelastic Earth: theory for finite faults and application to the 1964 Alaska earthquake, *J. geophys. Res.,* **102**(B1), 477–492.

Pollitz, F.F., 1996. Coseismic deformation from earthquake faulting on a layered spherical Earth, *Geophys. J. Int.,* **125**(1), 1–14.

Pollitz, F.F., Bürgmann, R. & Banerjee, P., 2006. Post-seismic relaxation following the great 2004 Sumatra–Andaman earthquake on a compressible self-gravitating Earth, *Geophys. J. Int.,* **167**(1), 397–420.

Pollitz, F.F. *et al.*, 2011. Coseismic slip distribution of the February 27, 2010 M_w 8.8 Maule, Chile earthquake, *Geophys. Res. Lett.,* **38,** L09309.

Sabadini, R. & Vermeersen, L., 1997. Influence of lithospheric and mantle stratification on global post-seismic deformation, *Geophys. Res. Lett.,* **24**(16), 2075–2078.

Sabadini, R., Piersanti, A. & Spada, G., 1995. Toroidal/poloidal partitioning of global post-seismic deformation, *Geophys. Res. Lett.,* **22**(8), 985–988.

Shan, B., Xiong, X., Zheng, Y. & Diao, F., 2009. Stress changes on major faults caused by M_w 7.9 Wenchuan earthquake, May 12, 2008, *Sci. China,* **52**(5), 593–601.

Shen, W., Yang, Z., Guo, Z. & Zhang, W., 2019. Numerical solutions of rotational normal modes of a triaxial two-layered anelastic Earth, *Geod. Geodyn.,* **10**(2), 118–129.

Singh, S.J., 1970. Static deformation of a multilayered half-space by internal sources, *J. geophys. Res.,* **75**(17), 3257–3263.

Soldati, G., Piersanti, A. & Boschi, E., 1998. Global postseismic gravity changes of a viscoelastic Earth, *J. geophys. Res.,* **103**(B12), 29 867–29 885.

Sun, W. & Okubo, S., 1993. Surface potential and gravity changes due to internal dislocations in a spherical Earth, I. Theory for a point dislocation, *Geophys. J. Int.,* **114**(3), 569–592.

Sun, W. & Okubo, S., 2002. Effects of earth's spherical curvature and radial heterogeneity in dislocation studies—for a point dislocation, *Geophys. Res. Lett.,* **29**(12), doi:10.1029/2001GL014497.

Sun, W., Okubo, S., Fu, G. & Araya, A., 2009. General formulations of global co-seismic deformations caused by an arbitrary dislocation in a spherically symmetric earth model—applicable to deformed earth surface and space-fixed point, *Geophys. J. Int.,* **177,** 817–833.

Takagi, Y. & Okubo, S., 2017. Internal deformation caused by a point dislocation in a uniform elastic sphere, *Geophys. J. Int.,* **208,** 973–991.

Takeuchi, H. & Saito, M., 1972. Seismic surface waves, *Methods Comput. Phys.,* **11,** 217–295.

Tanaka, Y., Okuno, J. & Okubo, S., 2006. A new method for the computation of global viscoelastic post-seismic deformation in a realistic earth model

(I)—vertical displacement and gravity variation, *Geophys. J. Int.,* **164**(2), 273–289.

Tanaka, Y., Okuno, J. & Okubo, S., 2007. A new method for the computation of global viscoelastic post-seismic deformation in a realistic earth model (II)—horizontal displacement, *Geophys. J. Int.,* **170,** 1031–1052.

Wang, R., Martin, F.L. & Roth, F., 2003. Computation of deformation induced by earthquakes in a multi-layered elastic crust—FORTRAN programs EDGRN/EDCMP, *Comput. Geosci.,* **29,** 195–207.

Wang, R., Martin, F.L. & Roth, F., 2006. PSGRN/PSCMP—a new code for calculating co- and post-seismic deformation, geoid and gravity changes based on the viscoelastic-gravitational dislocation theory, *Comput. Geosci.,* **32,** 527–541.

Zhou, X., Cambiotti, G., Sun, W. & Sabadini, R., 2014. The coseismic slip distribution of a shallow subduction fault constrained by prior information: the example of 2011 Tohoku (M_w9.0) megathrust earthquake, *Geophys. J. Int.,* **199**(2), 981–995.

Zhou, X., Cambiotti, G., Sun, W. & Sabadini, R., 2018. Co-seismic slip distribution of the 2011 Tohoku (M_w 9.0) earthquake inverted from GPS and space-borne gravimetric data, *Earth Planet. Phys.,* **2,** 120–138.